# Stellar $(n, \gamma)$ cross sections of $^{174}$Hf and radioactive $^{182}$Hf

C. Vockenhuber*
*TRIUMF, 4004 Wesbrook Mall, Vancouver, British Columbia, Canada V6T 2A3*

I. Dillmann,† M. Heil, F. Käppeler, and N. Winckler
*Institut für Kernphysik, Forschungszentrum Karlsruhe, Postfach 3640, D-76021 Karlsruhe, Germany*

W. Kutschera and A. Wallner
*Vienna Environmental Research Accelerator (VERA), Institut für Isotopenforschung und Kernphysik, Universität Wien, Währinger Strasse 17, A-1090 Wien, Austria*

M. Bichler
*Atominstitut der Österreichischen Universitäten, Stadionallee 2, A-1020 Wien, Austria*

S. Dababneh
*Faculty of Science and Information Technology, Al-Balqa Applied University, P.O. Box 7051, Salt 19117, Jordan*

S. Bisterzo‡ and R. Gallino§
*Dipartimento di Fisica Generale, Università di Torino and Sezione INFN di Torino, I-10125 Torino, Italy*
(Received 18 August 2006; revised manuscript received 22 November 2006; published 12 January 2007)

The stellar neutron capture cross sections of $^{174}$Hf and the radioactive isotope $^{182}$Hf ($t_{1/2} = 8.9 \times 10^6$ yr) have been measured for the first time at $kT = 25$ keV by means of the activation technique. These isotopes originate from different stellar scenarios, $^{174}$Hf from the $p$-process by a series of photodisintegration reactions of heavier seed nuclei, and $^{182}$Hf from the $s$-process in asymptotic giant branch stars as well as from the $r$-process in supernovae or neutron star mergers. Both activation measurements were carried out at the Karlsruhe Van de Graaff accelerator using the $^7$Li$(p, n)^7$Be reaction for simulating a Maxwellian neutron spectrum corresponding to a thermal energy of $kT = 25$ keV. The Maxwellian averaged cross sections (MACS) extrapolated to the common $s$-process temperatures at $kT = 30$ keV yield $\langle\sigma\rangle_{30} = 983 \pm 46$ and $141 \pm 8$ mb for $^{174}$Hf and $^{182}$Hf, respectively.

DOI: 10.1103/PhysRevC.75.015804 PACS number(s): 25.40.Lw, 26.30.+k, 27.70.+q, 97.10.Cv

## I. INTRODUCTION

The isotopic abundance pattern of hafnium contains plenty of information concerning the nucleosynthesis scenarios for the heavy elements. In the first place, this holds for the main $s$-process component produced in thermally pulsing, low-mass asymptotic giant branch (AGB) stars [1], which is responsible for the $s$ abundances between Sr and the Pb/Bi isotopes. The reaction path sketched in Fig. 1 shows that the hafnium isotopes are connecting the elements lutetium, tantalum, and tungsten, each of which is of special importance to nucleosynthesis studies.

The $s$-only isotope $^{176}$Hf is shielded against the $\beta$-decay chains of the $r$-process by its stable isobars $^{176}$Yb and $^{176}$Lu. It is produced partly by neutron captures on $^{175}$Lu feeding the short-lived isomer in $^{176}$Lu ($t_{1/2} = 3.68$ h) and partly by the decay of the very long-lived $^{176}$Lu ground state ($t_{1/2} \sim 37$ Gyr). Originally the decay of the ground state was considered as a potential clock for the age of the $s$ elements [2,3]. However, it was suspected [4] and later confirmed [5] that the energetic thermal photon bath at the $s$-process temperatures of typically $3 \times 10^8$ K leads to partial equilibration in the population of ground state and isomer, and hence to a drastic reduction of the effective stellar half-life of $^{176}$Lu, thus converting the cosmic clock into a stellar thermometer.

At $A = 179/180$, the puzzling origin of the rarest stable isotope in nature, $^{180}$Ta$^m$, has been and still is intensively studied with respect to different scenarios. Among those, the $s$-process allows one to reproduce most of $^{180}$Ta in a rather quantitative way [6,7], but significant abundance contributions were also found in recent studies of the $p$-process [8,9], whereas the $\nu$-process [10] has been shown to add only a small fraction to the $^{180}$Ta abundance [7]. The $s$-process production of this extremely rare isotope proceeds through very weak branchings in the nuclear reaction path. The first branching occurs at $^{179}$Hf, which becomes unstable at stellar temperatures because of $\beta$ decays from thermally populated excited states [11], thus contributing to the production of $^{180}$Ta

*Electronic address: christof.vockenhuber@triumf.ca; also at Simon Fraser University, Burnaby, British Columbia, Canada V5A 1S6.
†Also at Departement für Physik und Astronomie, Universität Basel, Switzerland.
‡Also at Institut für Kernphysik, Forschungszentrum Karlsruhe, Postfach 3640, D-76021 Karlsruhe, Germany.
§Also at Centre for Stellar and Planetary Astrophysics, Monash University, Victoria 3800, Australia.

 

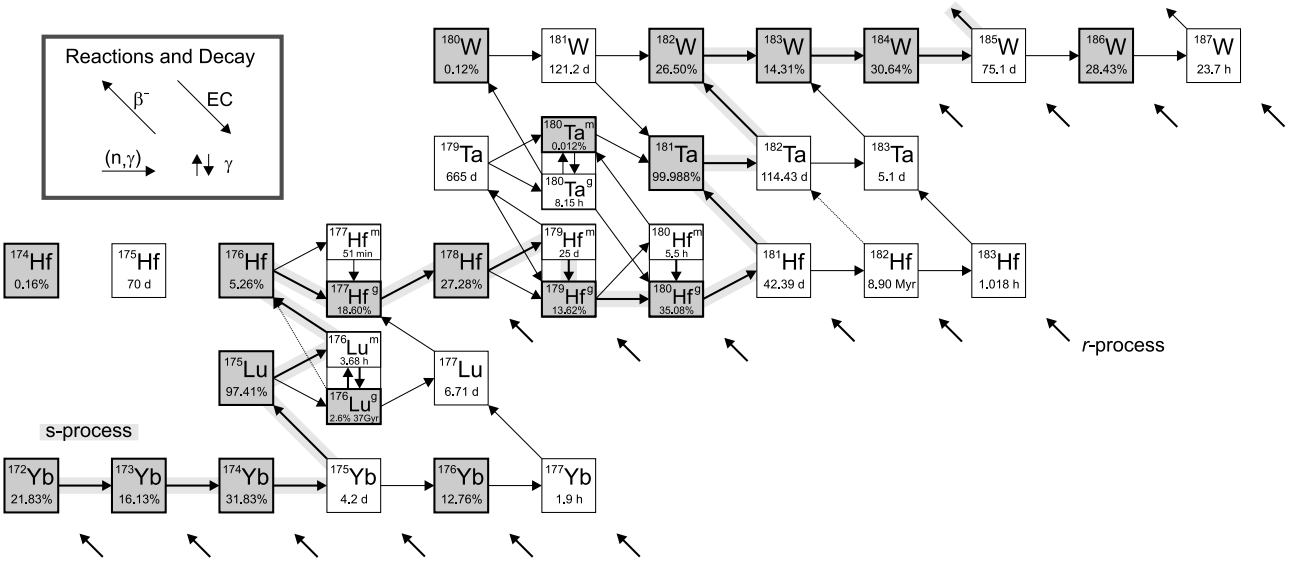


FIG. 1. Reaction path of the *s*-process in the region of hafnium isotopes. Relevant isomeric states are indicated by separate boxes. Main *s*-process follows the shaded path; *r*-process contributions are indicated by short arrows. Note the *s*-only pair $^{176}$Lu and $^{176}$Hf, which is shielded against $\beta$ decays from the *r*-process region by $^{176}$Yb. Similarly, $^{180}$Ta$^{m}$ and $^{180}$W are shielded by $^{180}$Hf.

by subsequent $(n, \gamma)$ reactions on $^{179}$Ta. The second branching proceeds via neutron captures on $^{179}$Hf, feeding a high-spin isomer in $^{180}$Hf, which then decays to $^{180}$Ta$^{m}$ [12]. Because of the intricate nuclear physics involved, the production of $^{180}$Ta$^{m}$ represents a sensitive test for the thermodynamics of He shell flashes in thermally pulsing low-mass AGB stars [6,13].

From the experimental point of view, these aspects have been recently stimulated by accurate cross section measurements on the main stable isotopes [14], including the effect of several isomeric states (Fig. 1). The present experiment aims at complementing these data by measurements on $^{174}$Hf and $^{182}$Hf, which represent the far ends of the (stable and long-lived) isotope chain.

The lightest isotope, $^{174}$Hf, originates from the so-called $\gamma$-process or *p*-process, which is responsible for the formation of the 32 very rare stable isotopes on the proton-rich side of the stability valley. What these *p* nuclei have in common is that they cannot be produced by neutron capture. Therefore, they lie either outside the reaction path of the *s*-process or are shielded by stable isobars against the $\beta$-decay chains from the *r*-process region (Fig. 1).

The *p*-process is commonly ascribed to explosive nucleosynthesis in supernovae, when the Ne/O layers of the pre-supernova star are heated to ignition temperatures by the outgoing shock front. Ne/O burning leads to peak temperatures of $10^9$ K, resulting in the production of proton-rich isotopes via photodisintegration reactions on the heavy seed nuclei in this layer. For describing this scenario, a complex reaction network is required, which connects some 1800 nuclei with more than 15000 $(\gamma, n)$, $(\gamma, p)$, and $(\gamma, \alpha)$ reactions and their respective inverse reactions. The later decrease in temperature leads to freeze-out via neutron captures and $\beta^+$ decays, producing the typical *p*-process abundance pattern with maxima at $^{92}$Mo ($N = 50$) and $^{144}$Sm ($N = 82$) [15,16].

A major difficulty in treating this network properly is the persisting uncertainties of the nuclear reaction rates. So far, experimental information is rather scarce even for the stable *p* isotopes, but is completely missing for the unstable nuclei, which represent by far the dominant part of the network. This information can presently only be provided by theoretical calculations based on the statistical Hauser-Feshbach model. To validate the parametrization of this model for *p*-process applications, as much experimental data as possible has to be collected for the proton-rich nuclei. In this respect, a first measurement of the $(n, \gamma)$ cross section of $^{174}$Hf is important in itself. Moreover, the predictive power of the theoretical model can be tested by comparison with the measured cross sections of the full isotope chain up to $A = 182$.

On the neutron-rich side, the long-lived isotope $^{182}$Hf ($t_{1/2} = 8.9 \times 10^6$ yr [17]) can be produced in the *s*- as well as the *r*-process. As illustrated in Fig. 1, the ultimate *s*-process abundance is determined by the branching at $A = 181$. So far, the formation and destruction rates of the relevant unstable isotopes $^{181}$Hf and $^{182}$Hf have not been studied experimentally.

The separation of the *s* and *r* components is important for the discussion of the origin of the $^{182}$Hf abundance in the early solar system. Evidence for a high $^{182}$Hf abundance comes from $^{182}$W deficiencies in early segregated iron meteorites relative to the silicate Earth [18,19]. This is interpreted as an excess in the silicate Earth due to radiogenic growth of $^{182}$W from in-situ decay of now extinct $^{182}$Hf after core formation, because hafnium is retained in the silicate mantle while tungsten is largely partitioned into the core. Similarly, $^{182}$W excess has been found in meteoritic materials with high Hf/W ratios that segregated at an early stage. Although there have been several attempts to explain the abundance in connection with other extinct radionuclides (see, e.g., [20,21]), the origin of the high

$^{182}$Hf abundance in the early solar system remains an open question.

The improved assessment of the *s*-process production of $^{182}$Hf on the basis of an experimental cross section thus provides an important contribution to the chronometry of the early solar system [22].

The experimental determination of the $(n, \gamma)$ cross sections of $^{174}$Hf and $^{182}$Hf is described in Secs. II to IV, followed by a comparison with theoretical predictions (Sec. V) and a discussion of the astrophysical implications in Sec. VI.

## II. MEASUREMENTS

### A. Hf samples

For the $^{174}$Hf activations, thin samples (Hf-3 to Hf-5) were cut from metal foils of natural composition [23], whereas the $^{182}$Hf activations were carried out with samples Hf-1 and Hf-2, which were prepared from the original Helmer-2 sample [17] (Table I).

This original sample, which was produced by irradiation of hafnium in an intense thermal neutron flux by Helmer and Reich more than 30 years ago, served initially for the study of the high-spin isomer $^{178}$Hf$^{m2}$ [25] and later for the study of the decay of $^{182}$Hf to $^{182}$Ta ($t_{1/2} = 114$ d) [26]. These materials were recently prepared for the half-life measurement of $^{182}$Hf at the Department of Earth Sciences, ETH-Zurich, Switzerland, and split into four samples (for details see Ref. [17]). For the present experiment, we used one of the samples (B3) containing $2.861 \times 10^{16}$ $^{182}$Hf atoms with the isotopic composition listed in Table I.

The preparation of the actual sample was performed at the Atominstitut der Österreichischen Universitäten (ATI) in Vienna, Austria. A few days prior to the activations at keV neutron energies, tantalum and hafnium were separated by ion exchange to reduce the background in the region of the expected $^{183}$Hf $\gamma$-ray lines due to Compton scattering of $\gamma$ rays emitted in the decay of the $^{182}$Hf daughter $^{182}$Ta.

About 3 cm$^3$ of the strongly basic anion exchange resin Dowex 1X8 (mesh 200–400) [27] was prepared by immersion in a 1:1 mixture of 1*M* hydrofluoric and 1*M* nitric acid for 24 h. After transfer to the exchange column made from polypropylene, the resin was rinsed with tridistilled water and again with 100 ml of the acid mixture. Then 3 ml of sample B3 were added, followed again by the acid. After passing through the column, the solution was collected in steps of 3 ml in perfluoroalkoxy-polymer resin (PFA) screw cap vials and measured sequentially. The $\gamma$-ray line at 270 keV associated with the decay of the long-lived $^{182}$Hf was used for quantification of the hafnium yield. The first two extracts did not contain any detectable $^{182}$Hf. Extracts 3 to 6 yielded more than 99% of the $^{182}$Hf measured in the original sample B3. Further extraction produced only negligible traces of $^{182}$Hf. The total volume of 12 ml extracted solution was reduced by freeze drying to about 4 ml. This volume was added to 60 mg of high-purity graphite powder (Ultra "F" purity, Ultra Carbon, Bay City, Michigan) and dried in a 5 ml PFA vial by application of an infrared lamp in a laminar-flow clean bench.

From this mixture, two samples were pressed to form a disk 8 mm in diameter and 0.65 mm thick. Sample Hf-1 contained about 60% and sample Hf-2 about 40% of the original $^{182}$Hf content. The total losses during sample preparation amounted to about 1%.

The $^{182}$Hf samples were later used for neutron capture measurements at thermal energies which led also to a precise determination of the half-life and absolute $\gamma$ intensities of the main $\gamma$ lines of $^{183}$Hf [28,29].

TABLE I. Isotopic composition of the hafnium samples (in %).

| Isotope | Nat. abundance | Helmer-2 |
|---|---|---|
| $^{174}$Hf | $0.16 \pm 0.01$[a] | $0.00014 \pm 0.00003$ |
| $^{176}$Hf | $5.26 \pm 0.07$ | $4.3772 \pm 0.0003$ |
| $^{177}$Hf | $18.60 \pm 0.90$ | $0.1492 \pm 0.0002$ |
| $^{178}$Hf | $27.28 \pm 0.07$ | $17.1493 \pm 0.0006$ |
| $^{179}$Hf | $13.62 \pm 0.02$ | $31.3013 \pm 0.0011$ |
| $^{180}$Hf | $35.08 \pm 0.16$ | $46.910 \pm 0.003$ |
| $^{182}$Hf | – | $0.11237 \pm 0.00002$ |

[a]Best value: $0.1620 \pm 0.0009$ [24].

TABLE II. Sample characteristics.

| Sample | Diameter (mm) | Mass (mg) | $N_x$ ($10^{16}$ atoms) | | |
|---|---|---|---|---|---|
| | | | $^{174}$Hf | $^{180}$Hf | $^{182}$Hf |
| Hf-1 | 8 | 39.2[a] | 0.00231 | 772.8 | 1.851 |
| Hf-2 | 8 | 26.5[a] | 0.00124 | 414.1 | 0.992 |
| Hf-3 | 6 | 92.0 | 49.66 | 10890 | – |
| Hf-4 | 6 | 92.1 | 49.72 | 10900 | – |
| Hf-5 | 8 | 163.5 | 88.26 | 19350 | – |

[a]Sample Helmer-2 plus graphite.

### B. Activation at stellar energies

The measurements at keV neutron energies were carried out at the Forschungszentrum Karlsruhe (FZK) 3.7 MV Van de Graaff accelerator using the activation technique. Neutrons were produced with the $^7$Li$(p, n)^7$Be reaction by bombarding 30 $\mu$m thick layers of metallic Li or LiF on a water-cooled Cu backing with protons of 1912 keV, 30 keV above the reaction threshold. The resulting quasistellar neutron spectrum approximates a Maxwellian distribution for $kT = 25.0 \pm 0.5$ keV ($3 \times 10^8$ K) [30], but it is truncated at a neutron energy of 106 keV. Under these conditions, all neutrons are kinematically collimated into a forward cone with 120° opening angle. Neutron scattering through the Cu backing is negligible since the transmission is ~98% in the energy range of interest. As discussed in Ref. [30], a Maxwellian distribution for typical *s*-process temperatures at $kT = 30$ keV could be approximated by raising the proton energy, thus avoiding the extrapolation from $kT = 25$ keV to $kT = 30$ keV (see Sec. IV C). However, the neutron beam is then not collimated in the forward direction, and thus corrections for neutron scattering in the target area are necessary.

During the activation measurements, the Van de Graaff accelerator was operated in dc mode with a proton beam

current of ∼100 $\mu$A. To ensure homogeneous illumination of the entire surface, the proton beam was wobbled across the Li target. Activation of the samples was performed in close contact with the Li target at the position of the highest flux.

The samples were sandwiched between 30 $\mu$m thick gold foils of the same diameter. In this way, the neutron flux can be determined relative to the well-known capture cross section of $^{197}$Au [30]. Throughout the irradiations, the neutron flux history was recorded in intervals of 1 min using a $^{6}$Li-glass detector for later correction of the number of nuclei, which decayed during the activations [factor $f_b$ in Eq. (1)].

For the measurement of the induced activities, two detector setups were available. A single HPGe detector with a fixed measuring position 76 mm in front of the detector was used for counting the activity of the gold foils. The detector was shielded by 10 cm of lead and 5 mm of copper. Similar to the procedure described above, the absolute efficiency was measured with a set of calibrated reference sources. Interpolation to the 411.8 keV $\gamma$ line from the decay $^{198}$Au yielded a value of 0.219 ± 0.004%.

The lower activities of the hafnium samples were measured with a $\gamma$-detection system consisting of two HPGe Clover detectors, shown in Fig. 2. Each Clover detector consists of four independent HPGe $n$-type crystals in a common cryostat. The crystals are 50 mm in diameter and 70 mm long. In one of the Clovers, the front part of the crystals is slightly tapered. The total crystal volume of the detector system is about 1000 cm$^3$. In addition to a $\gamma$ shielding (10 cm of lead and 5 mm copper), thin plastic sheets in front of the detectors were used to absorb energetic decay electrons.

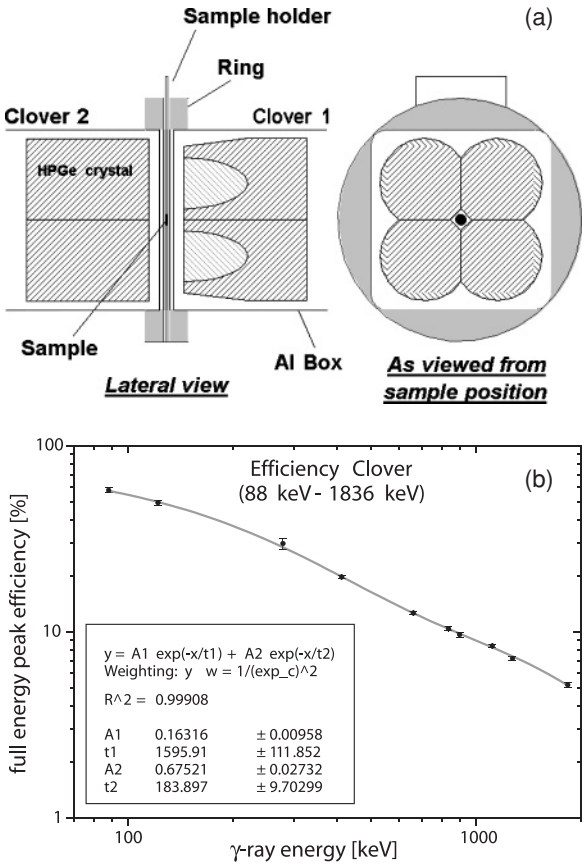


FIG. 2. (a): $\gamma$ detection system consisting of two HPGe Clover detectors with the irradiated sample in between. (b): Efficiency of the Clover system used.

The two Clover detectors are placed face to face in close geometry and form nearly a $4\pi$ array by touching the 5.2 mm thick sample holder. This holder is designed to guarantee an exact and reproducible positioning of the sample in the very center of the system. All crystals of the two Clovers have independent outputs, which are amplified via spectroscopy amplifiers with a shaping time of 6 $\mu$s. Each amplifier is connected to a 8192 channel analog-to-digital converter (ADC). The ADC signals are recorded in a personal computer, and events are analyzed via MPAWIN software. This tool kit allows one to visualize and analyze each spectrum independently. The total number of signals per $\gamma$ line is then derived by summation of the corresponding lines in all eight single spectra. Because of the high overall efficiency, a set of weak calibration sources [31] had to be used in measuring the efficiency of the Clover system (Fig. 2). The sum spectrum of sample Hf-1 accumulated in four activations is shown in Fig. 3.

## III. DATA ANALYSIS

After the irradiation, the number of activated atoms of nuclide $i$ is determined by

$$N(i) = N_x(i)\sigma(i)\Phi_{\text{tot}} f_b(i). \tag{1}$$

In this equation, $N_x(i)$ is the respective number of (stable or long-lived) nuclides $i$ in the sample, $\sigma(i)$ is the neutron capture cross section in the experimental neutron spectrum, and $\Phi_{\text{tot}} = \int \phi(t)\,dt$ the total, time-integrated neutron flux. The factor

$$f_b(i) = \frac{\int_0^{t_a} \phi(t) e^{-\lambda_i (t_a - t)} dt}{\int_0^{t_a} \phi(t) dt} \tag{2}$$

accounts for the decay of activated nuclei during the irradiation time $t_a$ as well as for variations in the neutron flux, and $\lambda_i$ denotes the respective decay constant of nuclide $i$. This factor is calculated from the neutron flux history recorded throughout the irradiation with the $^{6}$Li glass detector at a 91 cm distance from the target. The total number of activated nuclei $N(i)$ at the end of the irradiation can be deduced from the number of events $C_\gamma(i)$ in a particular $\gamma$-ray line registered in the $\gamma$ detector during the measuring time $t_m$ [32], that is,

$$N(i) = \frac{C_\gamma(i)}{\varepsilon_\gamma I_\gamma k_\gamma (1 - e^{-\lambda_i t_m}) e^{-\lambda_i t_w}}. \tag{3}$$

The factors $\varepsilon_\gamma$ and $I_\gamma$ account for the $\gamma$ efficiency and the absolute $\gamma$ intensity per decay of the respective transition, and $t_w$ denotes the waiting time between the irradiation and the activity measurement. The decay parameters used in the present analysis are given in Table III, which includes more precise values for the half-life of $^{183}$Hf and the absolute $\gamma$ intensities of the two main $\gamma$ lines obtained from the thermal irradiation [28,29].

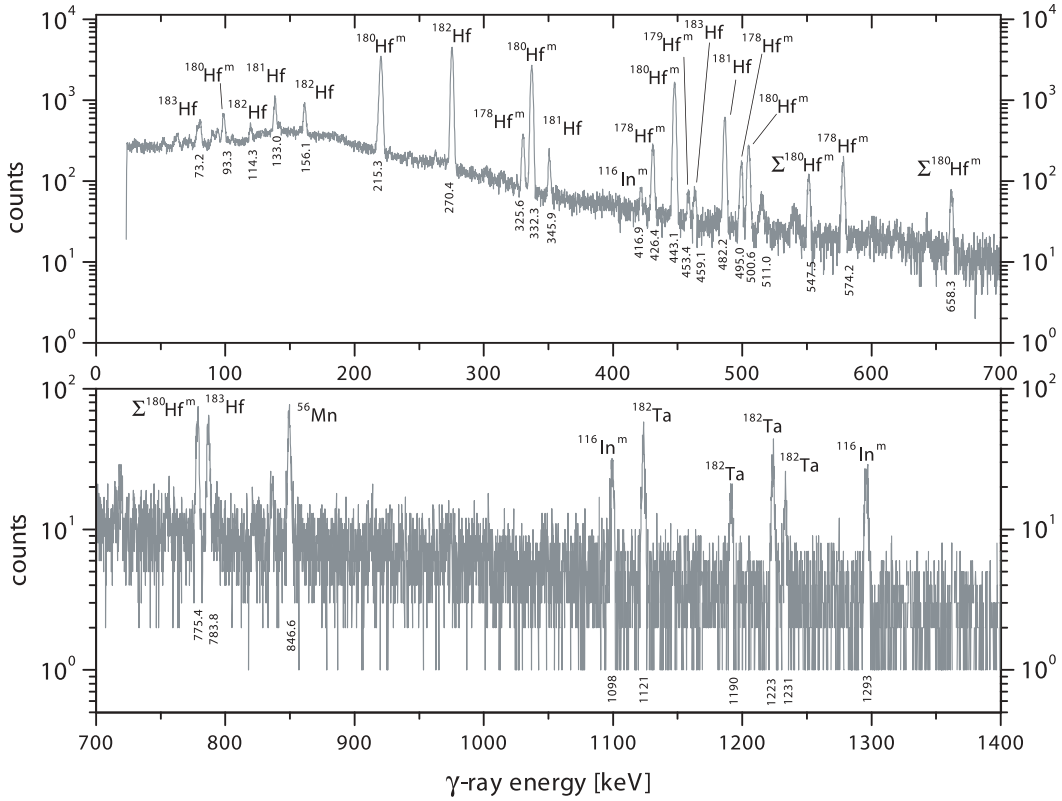


FIG. 3. Accumulated spectrum of sample Hf-1 after four irradiations in the quasistellar spectrum. Data were taken with the Clover detector (only one Ge crystal is shown). Main peaks and corresponding $\gamma$-ray energies are labeled ($\Sigma$ – sum peak).

The samples were activated in a series of irradiations, the respective $N(i)$ values from Eq. (3) were corrected for the surviving fraction of the preceding activation, $N_{\mathrm{prec}}(i)$, that is,

$$N_c(i) = N(i) - N_{\mathrm{prec}}(i)e^{-\lambda_i t_d}, \tag{4}$$

where $t_d$ is the duration of the cycle. This correction was only relevant for the calculation of the $^{181}$Hf activity.

TABLE III. Decay properties of the strongest transitions in the respective product nuclei.

| Nuclide | $t_{1/2}$ | $E_\gamma$ (keV) | $I_\gamma$ (%) | Ref. |
|---|---|---|---|---|
| $^{175}$Hf | 70 ± 2 d | 343.4 | 84 ± 3 | [33] |
| $^{181}$Hf | 42.39 ± 0.06 d | 133.0 | 43.31 ± 0.50 | [34] |
| | | 345.9 | 15.12 ± 0.12 | |
| | | 482.2 | 80.50 ± 0.11 | |
| $^{182}$Hf | (8.90 ± 0.09)×10$^6$ yr | 156.1 | 7.0 ± 0.2 | [17,35] |
| | | 270.4 | 79.0 ± 0.6 | |
| $^{183}$Hf | 1.018 ± 0.002 h | 73.2 | 38.4 ± 4.0 | [28,36] |
| | | 459.1 | 29.7 ± 0.9 | [29] |
| | | 783.8 | 65.5 ± 1.9 | [29] |
| $^{183}$Ta | 5.1 ± 0.1 d | 246.1 | 26.8 ± 1.4 | [36] |
| | | 354.0 | 11.23 ± 0.29 | |
| $^{198}$Au | 2.69517 ± 0.00021 d | 411.8 | 95.58 ± 0.12 | [37] |
| $^{95}$Zr | 64.032 ± 0.006 d | 724.2 | 44.17 ± 0.13 | [38] |
| | | 756.7 | 54.46 ± 0.10 | |
| $^{97}$Zr | 16.755 ± 0.013 h | 743.4 | 93.06 ± 0.16 | [39] |

The absorption of $\gamma$ rays in the sample is corrected by the factor $k_\gamma$, which is determined by the respective absorption coefficients $\mu$ (taken from [40]) and the sample thickness $l$ (in $\mu$g/cm$^2$). For the far counting geometry used for the gold samples, this correction was obtained in good approximation by

$$k_\gamma = \frac{(1 - e^{-\mu l})}{\mu l}, \tag{5}$$

although this expression is exactly valid only for radiation parallel to the axis of the disk-shaped samples.

Because of the close geometry in the Clover setup, $k_\gamma$ and the correction factors $k_E$ and $k_S$, which account for the extended geometry of the sample and the summing effect of the detector due to cascade transitions, have been calculated by means of Monte Carlo simulations using the GEANT4 software [41] (Table IV). In the following, these factors are combined as $k_{\mathrm{tot}} = k_\gamma k_E k_S$ to be used instead of $k_\gamma$.

Since the decay of $^{183}$Hf proceeds mainly via a 783.8/73.2 keV cascade, the latter transition was suppressed in the measurements with the Clover setup by mounting the sample between two indium absorber foils 0.65 mm thick. In this way, the summing corrections for $^{183}$Hf could be reduced. This is illustrated in Table IV by comparing the $k_S$ values with and without indium absorber. The correction factors for the extended sample geometry, $k_E$, are included in $k_{\mathrm{tot}}$, but are not shown explicitly since they were marginal in all cases.

TABLE IV. Correction factors used in analysis of Clover data. Effect of indium absorber for suppression of 73.2 keV transition is illustrated by comparison with values in last two lines.

| Nucleus | $E_\gamma$ (keV) | Sample | Thickness (mm) | Self absorption | | Summing | | Total correct. incl. $k_E$ | |
|---|---|---|---|---|---|---|---|---|---|
| | | | | $k_\gamma$ | $\Delta k_\gamma$ (%) | $k_S$ | $\Delta k_S$ (%) | $k_{\rm tot}$ | $\Delta k_{\rm tot}$ (%) |
| $^{181}$Hf | 482.2 | Hf-1 | 0.35 | 0.9386 | 0.21 | 0.9798 | 0.23 | 0.9197 | 0.23 |
| | | Hf-2 | 0.25 | 0.9383 | 0.21 | 0.9824 | 0.23 | 0.9215 | 0.23 |
| $^{182}$Hf | 270.4 | Hf-1 | 0.35 | 0.8822 | 0.16 | 1.0012 | 0.18 | 0.8841 | 0.18 |
| | | Hf-2 | 0.25 | 0.8858 | 0.16 | 1.0014 | 0.18 | 0.8866 | 0.18 |
| $^{183}$Hf | 73.2[a] | Hf-1 | 0.35 | 0.0866 | 0.29 | 0.9919 | 0.54 | 0.0860 | 0.47 |
| | 459.1 | Hf-1 | 0.35 | 0.9343 | 0.21 | 1.0047 | 0.35 | 0.9393 | 0.35 |
| | | Hf-2 | 0.25 | 0.9377 | 0.21 | 1.0038 | 0.35 | 0.9414 | 0.35 |
| | 783.8 | Hf-1 | 0.35 | 0.9551 | 0.26 | 0.9940 | 0.30 | 0.9511 | 0.30 |
| | | Hf-2 | 0.25 | 0.9578 | 0.26 | 0.9952 | 0.30 | 0.9487 | 0.30 |
| Without In | 73.2 | Hf-1 | 0.35 | 0.9334 | 0.12 | 0.9355 | 0.17 | 0.8737 | 0.17 |
| Without In | 783.8 | Hf-1 | 0.35 | 0.9941 | 0.26 | 0.9316 | 0.30 | 0.9278 | 0.30 |

[a]Transition not used for analysis.

The number of $^{182}$Hf atoms in samples Hf-1 and Hf-2 was determined via the 270 keV $\gamma$-ray line,

$$N_x(^{182}\mathrm{Hf}) = \frac{C_\gamma(^{182}\mathrm{Hf})}{I_\gamma \varepsilon_\gamma k_\gamma t_m \lambda_{^{182}\mathrm{Hf}}}. \quad (6)$$

The results from measurements with three different detectors (including measurements at the ATI [29]) are summarized in Table V.

The capture cross sections can be calculated from the measured data in two ways. In the first evaluation, the cross section is calculated as

$$\sigma(i) = \frac{N_{\rm c}(i)}{N_x(i) f_b(i) \Phi_{\rm tot}}, \quad (7)$$

with [Eq. (8)] the time-integrated neutron flux of the reference nuclide $j$,

$$\Phi_{\rm tot}(j) = \frac{N(j)}{N_{\rm s}(j) f_b(j) \sigma(j)}. \quad (8)$$

The activations at keV neutron energies were carried out with gold reference foils 30 $\mu$m thick. The accurate $^{197}$Au cross section of $\sigma(^{197}\mathrm{Au}) = 586 \pm 8$ mb [30] measured in the quasistellar spectrum of the $^7$Li$(p, n)^7$Be reaction was adopted as a standard. The integrated neutron flux $\Phi_{\rm tot}$ at the position of the sample was determined by averaging the induced activities of both gold foils. Seven independent activations were carried out with the $^{182}$Hf samples with integrated fluxes between 1.3 and 2.7 $\times$ $10^9$ $n$/cm$^2$ s (Table VI).

The second evaluation of the $^{182}$Hf$(n, \gamma)$ cross section was performed relative to the 482 keV $\gamma$-ray line from $^{181}$Hf:

$$\frac{\sigma(^{182}\mathrm{Hf})}{\sigma(^{180}\mathrm{Hf})} = \frac{N_c(^{183}\mathrm{Hf})}{N_c(^{181}\mathrm{Hf})} \frac{f_b(^{181}\mathrm{Hf})}{f_b(^{183}\mathrm{Hf})} R \left( \frac{^{180}\mathrm{Hf}}{^{182}\mathrm{Hf}} \right). \quad (9)$$

The isotopic ratio $R(^{180}\mathrm{Hf}/^{182}\mathrm{Hf}) = 417.46 \pm 0.08$ is reported in Ref. [17]. In this evaluation, the $^{181}$Hf and $^{183}$Hf activities are derived from the same spectrum, thus eliminating systematic uncertainties from differences in the neutron flux seen by the sample or with respect to neutron flux standards, efficiency variations, and dead-time corrections. The $^{180}$Hf reference cross section for $kT = 25$ keV was adopted from a precise time-of-flight measurement by Wisshak *et al.* [14]. The energy-dependent cross section given there was folded with the experimental neutron distribution and yielded $\sigma_{\rm exp}(^{180}\mathrm{Hf}) = 159.8 \pm 2.0$ mb.

## IV. RESULTS AND DISCUSSION

### A. Experimental cross sections at $kT = 25$ keV

In an astrophysical environment with temperature $T$, the neutron spectrum corresponds to a Maxwell-Boltzmann distribution. The experimental neutron spectrum of the $^7$Li$(p, n)^7$Be

TABLE V. Determination of $^{182}$Hf content with different detectors.

| Sample | Total mass | $N_x(^{182}\mathrm{Hf})$ ($10^{16}$ atoms)[a] | | | | |
|---|---|---|---|---|---|---|
| | | FZK HPGe | FZK Clover | ATI HPGe[b] | Weighted mean | Adopted value[c] |
| Hf-1 | 39.2 mg | 1.821 $\pm$ 0.042 | 1.884 $\pm$ 0.038 | 1.842 $\pm$ 0.042 | 1.851 $\pm$ 0.023 | 1.851 $\pm$ 0.050 |
| Hf-2 | 26.5 mg | 0.924 $\pm$ 0.042 | 1.009 $\pm$ 0.020 | 0.991 $\pm$ 0.021 | 0.992 $\pm$ 0.018 | 0.992 $\pm$ 0.029 |

[a]Only uncertainties from $C_{270}(^{182}\mathrm{Hf})$ and $\varepsilon_{270}$ included.
[b]See Ref. [29].
[c]All uncertainty components included.

TABLE VI. Parameters of activations at FZK. Variations of integrated neutron flux and irradiation time are important for the assessment of systematic uncertainties.

| Nuclide | Sample/activation | $t_a$ (min) | $f_b$ | $\Phi_{tot}$[a] ($10^{12} n/cm^2$) |
|---|---|---|---|---|
| $^{182}$Hf | Hf-1 / a | 64.5 | 0.71 | $5.56 \pm 0.07$ |
| | Hf-1 / b | 113.7 | 0.56 | $17.35 \pm 0.11$ |
| | Hf-1 / c | 118.0 | 0.55 | $16.27 \pm 0.05$ |
| | Hf-1 / d | 152.0 | 0.47 | $19.63 \pm 0.09$ |
| | Hf-2 / e | 117.5 | 0.55 | $9.41 \pm 0.10$ |
| | Hf-2 / f | 115.7 | 0.55 | $15.81 \pm 0.12$ |
| | Hf-2 / g | 130.0 | 0.52 | $17.59 \pm 0.11$ |
| $^{174}$Hf | Hf-3 / h | 5440 | 0.98 | $869 \pm 12$ |
| | Hf-4 / i | 3865 | 0.99 | $604 \pm 8$ |
| | Hf-5 / k | 5451 | 0.98 | $509 \pm 7$ |

[a]Uncertainty includes contributions from $C_{412}(^{197}\text{Au})$, $I_{412}(^{197}\text{Au})$, and $\sigma(^{197}\text{Au})$.

reaction approximates the Maxwellian distribution

$$\Phi \sim E_n e^{-E_n/kT}, \tag{10}$$

at $kT = 25$ keV almost perfectly [30]. This spectrum is quite typical for $s$-process environments where neutrons are produced by $^{22}\text{Ne}(\alpha, n)^{25}\text{Mg}$ reactions. The cutoff in the experimental spectrum at 106 keV requires a correction for obtaining the exact Maxwellian averaged cross sections (MACS), $\langle\sigma\rangle_{kT} = \frac{\langle\sigma\upsilon\rangle}{\upsilon_T}$ at $kT = 25$ keV ($\upsilon_T = \sqrt{2kT/\mu}$ is the most probable velocity and $\mu$ the reduced mass). The correction can be determined by normalization of the corresponding energy-dependent cross section. Since the energy dependence is quite robust, the differential cross section $\sigma(E_n)$ from an existing database, e.g., JEFF, JENDL, or ENDF/B, can be folded with the experimental neutron spectrum to define the normalization factor $NF = \frac{\sigma}{\sigma_{exp}}$. With this normalization, MACS can then be calculated as a function of temperature $T$ or thermal energy $kT$ as

$$\frac{\langle\sigma\rangle_{kT}}{NF} = \frac{2}{\sqrt{\pi}} \frac{\int_0^\infty \sigma(E_n) E_n e^{-E_n/kT} dE_n}{\int_0^\infty E_n e^{-E_n/kT} dE_n}. \tag{11}$$

### 1. $^{174}Hf(n, \gamma)$

This cross section was obtained via the most intense $\gamma$-ray line in the decay of $^{175}$Hf at 343.4 keV. Figure 4 shows the separation of this line from the overlapping contribution of a stronger line at 345.9 keV from the decay of $^{181}$Hf, using a fit function consisting of two Gaussians and a linear background. The results from three activations were found to be in very good agreement (Table VII), yielding an average cross section for the experimental spectrum, $\sigma_{exp} = 990 \pm 46$ mb.

### 2. $^{180}Hf(n, \gamma)$

The stellar cross section of $^{180}$Hf was determined for all five samples relative to gold to check for consistency with the accurate cross section given in Ref. [14] obtained in a time-of-flight (TOF) experiment. Folding these results with

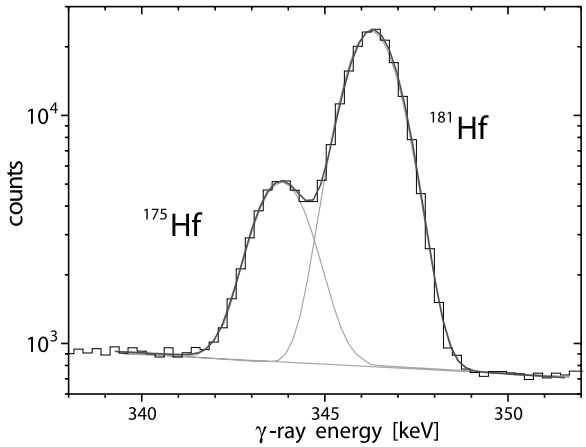


FIG. 4. Fit of $\gamma$-ray spectrum after irradiation of a natural hafnium sample. Overlapping lines at 343.4 and 345.9 keV are from the decay of $^{175}$Hf and $^{181}$Hf, respectively.

the quasistellar neutron spectrum used in the activations, one obtains a value of $159.8 \pm 2.0$ mb. The $\gamma$-ray spectra taken from the activated samples have been analyzed by using only the strongest transition in the decay of $^{181}$Hf at 482 keV. The resulting weighted average (Table VII) of $\sigma_{exp} = 158 \pm 7$ mb is in perfect agreement with the value based on the data of Ref. [14]. Analysis of the 345.9 keV line in Fig. 4 yields a $^{180}$Hf cross section consistent with this value, thus confirming the proper separation of the two lines in the fit of Fig. 4.

### 3. $^{182}Hf(n, \gamma)$

The $^{182}$Hf samples were irradiated several times for 2 h (except Hf-1/a, which lasted only 1 h), and the induced $^{183}$Hf activities were measured for 3 h in order to reduce the statistical uncertainty. The first two activations, Hf-1/a and Hf-2/e, show large discrepancies because the low counting statistics made the peak fits very uncertain.

The $^{182}$Hf cross section was determined relative to $^{197}$Au as well as relative to $^{180}$Hf as described in the previous section. The analysis was carried out by means of the two strongest transitions at 459 and 784 keV. The weighted mean of the results derived from both $\gamma$-ray lines and all activations yields experimental values of $144.4 \pm 8.0$ and $139.4 \pm 7.1$ mb if the normalization is made with respect to the cross section of $^{197}$Au

TABLE VII. Cross sections of $^{174}$Hf and $^{180}$Hf measured in quasistellar neutron spectrum.

| Sample / activation | $\sigma_{exp}$ (mb)[a] | |
|---|---|---|
| | $^{174}\text{Hf}(n, \gamma)$ | $^{180}\text{Hf}(n, \gamma)$ |
| Hf-1 / a-d | – | $161.5 \pm 6.1$ |
| Hf-2 / e-g | – | $166.4 \pm 6.4$ |
| Hf-3 / h | $985 \pm 45$ | $158.7 \pm 4.6$ |
| Hf-4 / i | $980 \pm 45$ | $151.5 \pm 4.4$ |
| Hf-5 / k | $1005 \pm 47$ | $157.6 \pm 4.5$ |
| Weighted mean: | $990 \pm 26$ | $157.9 \pm 2.2$ |

[a]Uncertainties are only due to counting statistics.

TABLE VIII. Cross sections of $^{182}$Hf measured in quasistellar neutron spectrum relative to $^{197}$Au and $^{180}$Hf.

| Sample/activation | $\sigma_{exp}$ (mb)[a] | |
|---|---|---|
| | $E_\gamma = 459$ keV | $E_\gamma = 784$ keV |
| Analysis relative to $^{197}$Au | | |
| Hf-1 / a | 103.9 ± 12.0 | 105.6 ± 8.8 |
| Hf-2 / e | 187.8 ± 25.2 | 152.7 ± 16.0 |
| Hf-1 / b | 150.3 ± 11.7 | 160.6 ± 4.9 |
| Hf-2 / f | 148.7 ± 14.7 | 146.2 ± 8.2 |
| Hf-1 / c | 146.2 ± 11.0 | 148.0 ± 5.4 |
| Hf-2 / g | 133.8 ± 16.9 | 131.4 ± 6.8 |
| Hf-1 / d | 157.7 ± 9.8 | 143.1 ± 4.9 |
| Weighted mean: | 143.6 ± 8.1 | 144.6 ± 5.2 |
| Analysis relative to $^{181}$Hf | | |
| Hf-1 / a | 106.9 ± 13.0 | 108.6 ± 9.9 |
| Hf-2 / e | 181.5 ± 24.8 | 147.6 ± 16.0 |
| Hf-1 / b | 141.3 ± 11.3 | 151.1 ± 5.4 |
| Hf-2 / f | 142.9 ± 14.9 | 140.5 ± 9.1 |
| Hf-1 / c | 143.3 ± 11.6 | 145.1 ± 6.8 |
| Hf-2 / g | 124.5 ± 16.5 | 122.3 ± 8.1 |
| Hf-1 / d | 154.2 ± 10.7 | 139.9 ± 6.4 |
| Weighted mean: | 139.7 ± 7.1 | 139.4 ± 4.8 |

[a]Uncertainties are only due to counting statistics.

or $^{180}$Hf, respectively. This very good agreement provides an important cross-check between TOF and activation data and confirms that both techniques yield consistent results.

Because in the past nearly every stellar neutron cross section measurement was carried out relative to $^{197}$Au [30,42], we consider our final result to be $\sigma_{exp}(^{182}\text{Hf}) = 144 \pm 8$ mb (Table VIII).

#### *4. Uncertainties*

The experimental uncertainties for the measurements at FZK are summarized in Table IX. Common to all measurements one finds substantial contributions due to the $\gamma$-ray efficiency $\varepsilon_\gamma$ and to the corrections $k_{tot}$, which are related to $\gamma$-ray absorption and to the close counting geometry.

In the case of the $^{174}$Hf cross section, the largest contributions are the error in the half-life and the 3.6% uncertainty in the $\gamma$-ray intensity. The uncertainties introduced by the time factor $f_b$ are always negligible, except for $^{175}$Hf because of the 2.9% uncertainty in the half-life. The isotopic abundance of $^{174}$Hf was taken from Ref. [24] instead of the rather uncertain value in the compilation of Ref. [23] (6.25% uncertainty).

For the $^{182}$Hf cross section, the overall uncertainty is dominated by the contribution from the (improved) $\gamma$-ray intensities [29] and by the counting statistics.

### B. Energy-dependent cross sections

Energy-dependent cross sections for $^{174}$Hf and $^{180}$Hf were available from the online data libraries JEF and JEFF (www.nea.fr/html/dbdata/JEFF/), JENDL (wwwndc.tokai-sc.jaea.go.jp/jendl/jendl.html), and ENDF/B-VI.8 (www.nndc.bnl.gov/), which are partially based on experimental resonance parameters. The cross sections of the libraries have been folded with the quasistellar spectrum. The results are compared in Table X together with theoretical predictions from the statistical model codes NON-SMOKER [43], TALYS [44], and EMPIRE [45]. Corresponding normalization factors (*NF*s) are also shown. Figure 5 illustrates the energy dependence of the cross section from different data libraries and theoretical predictions for $^{174}$Hf and $^{182}$Hf.

TABLE IX. Compilation of uncertainties for the activations at FZK.

| Source of uncertainty | Relative uncertainty (%) |
|---|---|
| Absorption effects, $k_{tot}$ | 2.0 |
| $\gamma$-Efficiency, $\varepsilon_\gamma$ | 2.0 |
| Integrated neutron flux, $\Phi_{tot}$ | 2.0 |
| Number of sample atoms, $N_x(^{182}\text{Hf})$ | 2.5 |
| $N_x(^{174}\text{Hf})$ | 0.56 |
| Counting statistics, $C_\gamma(^{175}\text{Hf})$ | 2.1–3.2 |
| $C_\gamma(^{181}\text{Hf})$[a] | 2.0–4.3 |
| $C_\gamma(^{182}\text{Hf})$ | 0.3 |
| $C_\gamma(^{183}\text{Hf})$[a] | 6.2–13.4 |
| Decay intensity, $I_\gamma(^{175}\text{Hf})$ | 3.6 |
| $I_\gamma(^{181}\text{Hf})$ | 0.14 |
| $I_\gamma(^{182}\text{Hf})$ | 0.76 |
| $I_\gamma(^{183}\text{Hf})$ | 2.9 |
| $I_\gamma(^{198}\text{Au})$ | 0.1 |
| Time factor, $f_b(^{175}\text{Hf})$ | 0.2 |
| Reference cross section, $\sigma_{exp}(^{180}\text{Hf})$ | 1.2 |
| $\sigma_{exp}(^{197}\text{Au})$ | 1.4 |
| | Overall uncertainty |
| $\sigma_{exp}(^{174}\text{Hf})$ | 4.6 |
| $\sigma_{exp}(^{180}\text{Hf})$ | 4.4 |
| $\sigma_{exp}(^{182}\text{Hf})$ | 5.5 |

[a]For single activations.

The $(n, \gamma)$ cross sections of $^{174}$Hf listed in JEFF/3.1 and JENDL/3.3 are almost identical between 1 eV $< E_n <$ 1 MeV; in both cases, resolved resonances are given in the energy

TABLE X. Cross sections (averaged over quasistellar neutron spectrum, in mb) and normalization factors derived from different databases and theoretical predictions.

| Database | $^{174}$Hf$(n,\gamma)$ | | $^{180}$Hf$(n,\gamma)$ | | $^{182}$Hf$(n,\gamma)$ | |
|---|---|---|---|---|---|---|
| | $\sigma_{25}$ | *NF* | $\sigma_{25}$ | *NF* | $\sigma_{25}$ | *NF* |
| Experiment ($\sigma_{exp}$) | 990 | 1.000 | 160 | 1.000 | 144 | 1.000 |
| Evaluations | | | | | | |
| JEF 2.2 | 1008 | 1.018 | 158 | 0.988 | – | – |
| JEFF 3.1 | 944 | 0.953 | 239 | 1.494 | – | – |
| JENDL 3.3 | 941 | 0.951 | 238 | 1.488 | – | – |
| ENDF/B-VI.8 | 686 | 0.692 | 177 | 1.106 | – | – |
| JEFF 3.0/A | | | | | 150 | 1.043 |
| Model calculations | | | | | | |
| NON-SMOKER | 769 | 0.777 | – | – | 104 | 0.722 |
| TALYS | 721 | 0.728 | – | – | 222 | 1.542 |
| EMPIRE | 1587 | 1.603 | – | – | 251 | 1.743 |

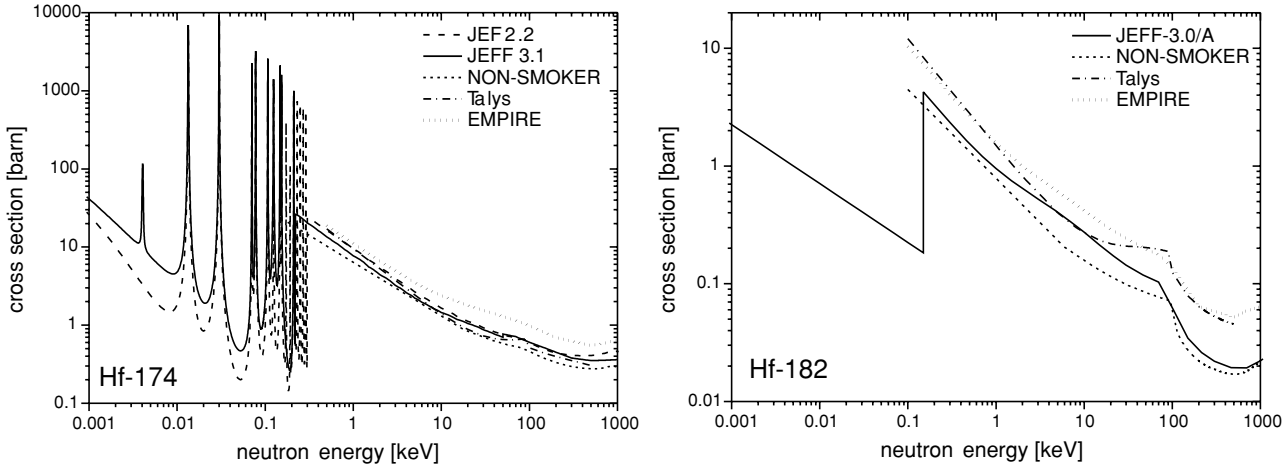


FIG. 5. Comparison of energy-dependent cross sections of $^{174}$Hf and $^{182}$Hf from available data libraries and theoretical predictions.

region below 0.2 keV. The data in ENDF/B-VI.8 differ only in the unresolved region, where the averaged cross section is almost 40% lower. Compared to the present experiment, normalization factors between 0.69 and 0.95 were found for the more recent evaluations, whereas a previous version (JEF/2.2) required a correction of only 2%. Theoretically predicted cross sections are worse in all cases and required *NF* values between 0.7 (TALYS) and 1.6 (EMPIRE).

Large discrepancies between JEFF/3.1 and JEF/2.2 were discovered for the $^{180}$Hf cross section as well. In the previous version, resolved resonances were considered between 0.1 and 11 keV, whereas the unresolved region in JEFF/3.1 starts already at 2.5 keV, and the energy dependence lies significantly above the accurate experimental values reported in Ref. [14]. The main differences are that JEFF/3.1 has adopted the resonance parameters between 0.2 and 2.5 keV from ENDF/B-VI and the unresolved cross sections between 2.5 and 50 keV from JENDL/3.3. Correspondingly, large normalization factors of 1.5 are required for the data listed in JEFF/3.1 and JENDL/3.3, whereas the previous version JEF/2.2 is in good agreement with the experimental data.

The $(n, \gamma)$ cross section of the unstable isotope $^{182}$Hf was not included in data libraries, except for JEFF-3.0/A. A first comparison with theoretical predictions from the statistical model codes NON-SMOKER, TALYS, and EMPIRE shows normalization factors between 0.7 and 1.7. A more detailed discussion follows in Sec. V.

### C. Maxwellian averaged cross sections

Table XI shows the Maxwellian averaged cross sections $\langle\sigma\rangle_{kT}$ of $^{174}$Hf and $^{182}$Hf for $kT = 5$–100 keV. The values were calculated according to Eq. (11) with the normalized JEF 2.2 cross section for $^{174}$Hf, whereas for $^{182}$Hf the normalized NON-SMOKER data were used (using JEFF-3.0/A for $^{182}$Hf gives very similar values). The semiempirical estimates from Ref. [42] are given for comparison.

Maxwellian averaged cross sections have to be corrected by a temperature-dependent stellar enhancement factor $SEF(T) = \frac{\sigma^{\text{star}}}{\sigma^{\text{lab}}}$. The stellar cross section $\sigma^{\text{star}} = \sum_\mu \sum_\nu \sigma^{\mu\nu}$ accounts for all transitions from excited target states $\mu$ to final states $\nu$ in thermally equilibrated nuclei, whereas the laboratory cross section $\sigma^{\text{lab}} = \sum_0 \sum_\nu \sigma^{0\nu}$ includes only captures from the target ground state. Tabulated *SEF*s can be found, e.g., in Refs. [42,43,46]. At a thermal energy of $kT = 30$ keV, these corrections are already 13% and 4% for $^{174}$Hf and $^{182}$Hf, respectively, and increase significantly with temperature (Table XI).

TABLE XI. Maxwellian averaged cross sections (in mb) and stellar enhancement factors [46] for $^{174}$Hf and $^{182}$Hf.

| $kT$ (keV) | 5 | 10 | 15 | 20 | 25 | 30 | 40 | 50 | 60 | 80 | 100 |
|---|---|---|---|---|---|---|---|---|---|---|---|
| | | | | | | MACS($^{174}$Hf) | | | | | |
| Bao *et al.* [42] | 2453 | 1436 | 1219 | 1100 | 1019 | 956 ± 283 | 863 | 797 | 746 | 674 | 625 |
| This work | 2797 | 1766 | 1394 | 1196 | 1071 | 983 ± 46 | 863 | 784 | 727 | 651 | 604 |
| *SEF* [46] | 1.000 | 1.001 | 1.012 | 1.044 | 1.088 | 1.133 | 1.207 | 1.261 | 1.304 | 1.377 | 1.442 |
| | | | | | | MACS($^{182}$Hf) | | | | | |
| Bao *et al.* [42] | 274 | 190 | 158 | 140 | 127 | 117 ± 41 | 101 | 88 | 79 | 65 | 56 |
| This work | 352 | 238 | 195 | 171 | 154 | 141 ± 8 | 120 | 104 | 92 | 75 | 64 |
| *SEF* [46] | 1.000 | 1.000 | 1.001 | 1.008 | 1.023 | 1.043 | 1.097 | 1.158 | 1.224 | 1.360 | 1.497 |

## V. THEORETICAL PREDICTIONS AND FUTURE PROSPECTS

Since the reaction networks for explosive nucleosynthesis, for the $p$- as well as the $r$-process, are located in the region of unstable nuclei, practically all necessary reaction rates have to be determined by statistical model calculations based on the Hauser-Feshbach approach. The predictive power of such calculations depends on the nuclear input used, which is commonly organized in the form of global parameter systematics derived from the comprehensive body of relevant properties for stable nuclei [46–48]. However, extrapolation of the systematics into the region of unstable nuclei represents a major problem.

An improvement of this situation has to rely on refined statistical model calculations. In this context, reference information obtained from long isotope chains provides an important test for the mass dependence of the calculations. The case of the hafnium isotopes was particularly suited for such a test since the $(n, \gamma)$ cross sections of both nuclei at the two ends of the chain, $^{174}$Hf and $^{182}$Hf, had not been measured before at stellar energies. Therefore, theoretical predictions at $kT = 25$ keV were invited prior to the experiments for later comparison with the measured data.

The summary of this comparison in Table XII indicates that statistical model calculations using carefully evaluated global parameter sets still exhibit the typical deficiencies of that approach. The various contributions, which had been promptly supplied in most cases, are listed in the order of submission. The results are quoted without further discussion of the parametrization, since a more detailed comparison is beyond the scope of this paper.

As far as the absolute cross sections are concerned, Table XII confirms that the predictive power of the various models is limited to the common ±30% agreement with experimental data [42]. It is interesting to note that the best agreement is obtained with the recommended values of Ref. [42], which were derived by comparing NON-SMOKER results to nearby experimental data.

TABLE XII. Theoretically predicted MACS at $kT = 25$ keV (in mb) compared with the experimental results for $^{174}$Hf and $^{182}$Hf. Ratio in last column indicates how well the mass dependence is reproduced. Notes indicate private communications.

| Entry | MACS$_{25\text{keV}}$ | | $^{174}$Hf/$^{182}$Hf (% exp. value) |
|---|---|---|---|
| | $^{174}$Hf | $^{182}$Hf | |
| 1- HFSM[a] | 690 ± 210 | 120 ± 35 | 5.8(82) |
| 2- NON-SMOKER[b] | 753 | 104 | 7.2(103) |
| 3- CoH[c] | 1055 ± 530 | 51 ± 25 | 20.7(296) |
| 4- TALYS[d] | 797 | 237 | 3.4(49) |
| 5- EMPIRE[e] | 1721 | 270 | 6.4(91) |
| 6- MOST [49] | 797 | 59 | 13.5(193) |
| Bao *et al.* [42] | 1019 | 127 | 8.0(114) |
| Measured data | 1071 ± 50 | 154 ± 9 | 7.0 ± 0.5 |

[a]A. Mengoni, IAEA Vienna.
[b]T. Rauscher, University of Basel.
[c]T. Kawano, Los Alamos National Laboratory.
[d]A. Koning, NRG Petten.
[e]M. Herman, NNDC Brookhaven.

Apart from the individual cross sections themselves, which are quite interesting, the more important information from Table XII is the cross section ratio of $^{174}$Hf and $^{182}$Hf, since it provides a measure of the cross section trend with neutron number. While the absolute cross sections can be normalized by means of known experimental data of stable isotopes, this trend is important for the extrapolation to the mass regions outside the stability valley.

Such extrapolations appear to be reliable only toward the $p$-process region, because the higher neutron separation energies on the proton-rich side give rise to high excitation energies of the compound system. Consequently, this favors the validity of the statistical model assumptions. Extrapolations toward the neutron-rich side are more problematic, since the decreasing neutron separation energies lead to increasing uncertainties in the statistical model parameters. This is also reflected in the large spread of the theoretically predicted cross sections for $^{182}$Hf. In summary, the comparison in Table XII confirms that statistical model calculations with global parameter sets covering a wide mass region are limited to uncertainties of 30% or more.

Consequently, experimental rates are indispensable for analyzing the abundance patterns in crucial $s$-process branchings. To meet this challenge, current experimental techniques have to be considerably improved. In the long run, cross section measurements on short-lived nuclei by the double neutron capture technique, e.g., via the sequence $^{180}$Hf$(n, \gamma)^{181}$Hf$(n, \gamma)^{182}$Hf, and subsequent counting of the unstable secondary product with accelerator mass spectrometry [50] will be possible with very intense neutron sources. Similar examples are the sequences $^{58}$Fe$(n, \gamma)^{59}$Fe$(n, \gamma)^{60}$Fe and $^{88}$Sr$(n, \gamma)^{89}$Sr$(n, \gamma)^{90}$Sr. Presently, experimental information can already be obtained by studying the $(\gamma, n)$ channel, starting from stable or long-lived nuclei. This approach, which was successfully used in several cases [51–53], allows one to significantly rectify the input for statistical model calculations.

For explosive nucleosynthesis, where the required accuracy is much less stringent than in case of the $s$-process, most of the data requests, e.g., for $p$-process calculations, can presumably be met by experiments with radioactive ion beams. First test runs have been made for $(\gamma, n)$ experiments in inverse kinematics with the LAND (large-array neutron detector) setup at GSI [54]. With this technique, a wide range of short-lived isotopes on both sides of the stability valley could be investigated. Nevertheless, theory will continue to play a key role in transforming these laboratory data into stellar rates and for interpolation between experimental data.

## VI. ASTROPHYSICAL IMPLICATIONS

The present result for the stellar $(n, \gamma)$ cross section of $^{182}$Hf represents an important step in the discussion of the unusual solar abundance pattern in the mass region $178 \leqslant A \leqslant 184$, where the decomposition into the $s$- and $r$-process components,

$$N_r = N_\odot - N_s,$$

is particularly intriguing. A recent analysis found that the minimum in the $r$-process abundances at $A = 180$ was much deeper than anticipated before, because the $s$ abundance of $^{180}$Hf was enhanced as a consequence of the smaller experimental cross section of that isotope [14]. This aspect is relevant for quantitative attempts to model the $r$-process, including the possible need for mixing $r$-process material from different sites (e.g., see Ref. [55,56]). The problem with this revision of the $r$-process abundance distribution was a significant deviation from the otherwise very smooth $r$-abundance pattern. It would be quite surprising if this deviation would indicate an inherent $r$-process feature. More likely it is expected to reflect uncertainties in the MACS governing the branchings at $^{181}$Hf and $^{182}$Ta shown in Fig. 1.

An important part of these uncertainties could be solved by means of the experimental $(n, \gamma)$ cross section of $^{182}$Hf. Furthermore, comparison with the theoretical calculations in Table XII shows that the cross section trend with neutron number beyond $A = 180$ appears to be less steep than predicted, suggesting that a $^{181}$Hf cross section of 300–400 mb may well be realistic. These changes in the stellar $(n, \gamma)$ cross sections have a significant impact on the final abundance pattern as it has been illustrated in Ref. [14] for the example of the $^{182}$W abundance.

The sensitivity of the abundance pattern to the branch point isotopes $^{181}$Hf and $^{182}$Ta was, therefore, studied by changing these cross sections within reasonable limits, while keeping the experimental values fixed. The adopted experimental data were (i) the present value for $^{182}$Hf, (ii) those of Ref. [14] for the stable hafnium isotopes, and (iii) the recommended values of Bao *et al.* [42] and more recent updates [57] for all the rest. Starting from this standard case, the cross sections of the critical cases were multiplied by factors of 0.7 and 1.3, but keeping the respective *SEF* values fixed [42]. As usual, the stellar $\beta$-decay rates were adopted from Ref. [11].

In a series of $s$-process calculations, the cross sections were changed one at a time. The stellar model used in this analysis [58,59] is characterized by the alternating activation of the $^{13}$C$(\alpha, n)$ and $^{22}$Ne$(\alpha, n)$ reactions during He shell burning in thermally pulsing, low-mass AGB stars. The $^{13}$C neutron source maintains a low neutron density in a very restricted mass layer—the so called $^{13}$C pocket—during a substantial part of the long H burning phase between He shell flashes, where temperatures are typically around $0.9 \times 10^8$ K. This reaction provides about 95% of the total neutron exposure. The $^{22}$Ne reaction is marginally activated at the higher temperatures of $(2.5–3.0)\times 10^8$ K that are reached at the bottom of the convective He shell flashes. Although high peak neutron densities of $\sim 10^{10}$ cm$^{-3}$ are reached in that stage, the contribution to the total neutron exposure is limited to about 5% because of the much shorter duration of this phase.

After the large neutron exposure in the interpulse period, which occurred radiatively, the pocket is completely engulfed by the subsequent He shell flash, and the abundance patterns that were formed in the $^{13}$C pocket are reshaped by the high-temperature, high-neutron-density burst during the He shell flash. This is particularly true for the region of the rare earth elements because the large cross sections of these isotopes facilitate the rapid adjustment of the abundance distribution during the final decrease of the neutron density. Accordingly, the isotope patterns of the branchings discussed below are completely defined during the He shell flashes.

TABLE XIII. Sensitivity of the $s$ and $r$ abundances of $^{181}$Ta and $^{182}$W with respect to cross section changes (abundances relative to Si $\equiv 10^9$).

| Adopted cross section | $s$ abundances | | $r$ residuals | |
|---|---|---|---|---|
| at $kT = 30$ keV | $^{181}$Ta | $^{182}$W | $^{181}$Ta | $^{182}$W[a] |
| Standard case old[b] | 9.43 | 21.9 | 11.3 | 13.1 |
| Standard case new[c] | 9.43 | 21.3 | 11.3 | 13.7 |
| MACS$_{^{181}\mathrm{Hf}} \times 1.3$ | 9.42 | 21.7 | 11.3 | 13.3 |
| MACS$_{^{181}\mathrm{Hf}} \times 0.7$ | 9.44 | 20.9 | 11.3 | 14.1 |
| MACS$_{^{182}\mathrm{Ta}} \times 1.3$ | 9.43 | 20.1 | 11.3 | 14.9 |
| MACS$_{^{182}\mathrm{Ta}} \times 0.7$ | 9.43 | 23.0 | 11.3 | 12.0 |
| MACS$_{^{182}\mathrm{W}} \times 1.3$ | 9.43 | 17.9 | 11.3 | 17.1 |
| MACS$_{^{182}\mathrm{W}} \times 0.7$ | 9.43 | 27.5 | 11.3 | 7.5 |

[a] After decay of $^{182}$Hf.
[b] MACS from Ref. [42] complemented with recent data for the stable hafnium isotopes [14].
[c] Cross section of $^{182}$Hf replaced by experimental value.

The result of this sensitivity study is summarized in Table XIII. The first column shows the various cases, starting with the standard case "old" based on the cross section data of Ref. [42], but updated for the cross sections of the stable hafnium isotopes [14]. The only difference to the standard case "new" was made by adopting the experimental value for $^{182}$Hf. The series was then continued by changing the cross sections of the branch point isotopes and of $^{182}$W itself by $\pm 30\%$.

Note that changes of the first branch point $^{181}$Hf have a negligible effect on the abundance of $^{181}$Ta, which means that the $s$ abundance is completely determined by the accurately known cross section of $^{181}$Ta. Since the $s$ abundance represents 45% of the solar value, the $r$ component of $^{181}$Ta is also well defined. As shown in Fig. 6, this results in an inversion of the odd-even effect in the $r$-process distribution, which is always favoring the abundances of the even isotopes. It seems that this puzzling situation may not be solved by revising the *SEF* value of $^{181}$Ta either, because it is presently estimated to be much too small for a plausible explanation.

The branching at $^{181}$Hf is marginal at He flash temperatures because the half-life of $^{181}$Hf is reduced by an order of magnitude as a result of thermal effects in the stellar plasma [11]. Accordingly, the contribution to the $^{182}$W abundance by the $s$-process production of $^{182}$Hf is reduced from 7.5% to 5.8% if the calculated $^{182}$Hf cross section listed in Ref. [42] is replaced by the new experimental value. This difference leads to a 2.6% change in the total $s$-process component of the $^{182}$W abundance (Table XIII). The effect of the branching at $^{182}$Ta on the $s$ component of $^{182}$W is also small. The 30% change of the cross section of this branch point isotope affects the $r$ component of $^{182}$W only by about 10%. The combined effect of the two branchings is illustrated in the inset of Fig. 6 by the smaller error bars on the left side of the $^{182}$W abundance (black rectangle).

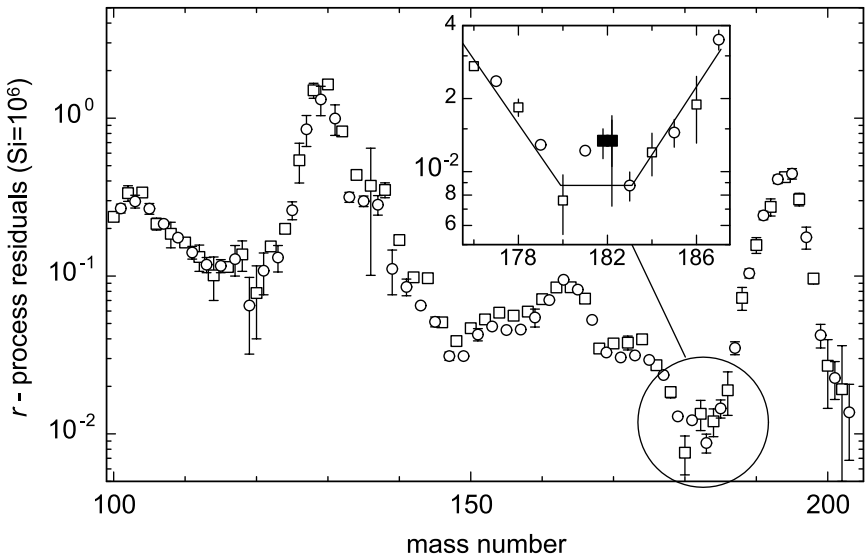


FIG. 6. $r$-process residuals $N_r = N_\odot - N_s$ between Ru and Pb for the odd and even isotopes (circles and squares, respectively). Previous data are from Ref. [59] updated by means of more recent cross sections [57] (open symbols). Inset illustrates the sensitivity of the $^{182}$W abundance (black rectangle) with respect to the $s$-process branchings at $^{181}$Hf and $^{182}$Ta (left error bars) and to the $^{182}$W cross section (right error bars). Error bars associated with the $^{182}$W abundance reflect the corresponding ±30% cross section variations used in the $s$-process calculations (Table XIII). A smooth $r$ distribution for the even isotopes suggests a low value for the $^{182}$W abundance, which could easily be obtained within present $s$-process uncertainties (see text).

In contrast, Table XIII indicates the $r$ abundance of $^{181}$Ta would easily fit into a smooth distribution if the stellar $^{182}$W cross section itself had been overestimated in the past. The effect of a 30% change is indicated in the inset of Fig. 6 by the larger error bars on the right side of the $^{182}$W abundance (black rectangle). This possibility appears, indeed, plausible, given the recent revision of the stellar $(n, \gamma)$ cross sections of $^{176}$Hf and $^{180}$Hf [14] and should be checked by an accurate measurement.

The production of $^{182}$Hf in AGB stars is of great relevance to the chronometry of the early solar system [22]. The $^{182}$Hf/$^{180}$Hf ratio in the early solar system was deduced from meteorite analyses by several groups, yielding values between (1.0 and 1.6) $\times 10^{-4}$ [60–64]. Of these values, the recent ratio of $(1.07 \pm 0.10) \times 10^{-4}$ reported in Ref. [65] for the time of formation of calcium-aluminum rich inclusions in chondritic material has been adopted for the following discussion. The difference between this value and the estimate of the $^{182}$Hf/$^{180}$Hf ratio in the protosolar cloud obtained with a simple model for uniform production [66] can be used for constraining the time $\Delta_1$ between the last synthesis event and the formation of solid parent bodies.

The original estimate of $4.8 \times 10^{-4}$ was obtained by adopting a 57% $r$-process component of solar $^{182}$W [58]. However, this value was recently challenged by revised cross section data [14], yielding a 37% lower $r$ abundance of $^{182}$W and, consequently, a reduction of the estimated $^{182}$Hf/$^{180}$Hf ratio to about $3 \times 10^{-4}$. This value would be further lowered to about $2 \times 10^{-4}$ if the $r$ abundance suggested by a smooth mass dependence (Fig. 6) were to be adopted. These changes imply that the corresponding values of $\Delta_1$ would be shortened from the original $19 \times 10^6$ yr to about $13 \times 10^6$ yr (for $3 \times 10^{-4}$) to about $8 \times 10^6$ yr (for $2 \times 10^{-4}$), respectively. To clarify this important problem, an accurate measurement of the stellar $(n, \gamma)$ cross section of $^{182}$W is urgently called for.

We note also that the estimated reduction of the $^{182}$Hf/$^{180}$Hf ratio and hence a shorter time $\Delta_1$ is still in sharp contrast to the longer time interval of $\Delta_1 \sim 10^8$ yr required to explain the much lower $^{107}$Pd and $^{129}$I abundances in the early solar system.

## VII. SUMMARY AND OUTLOOK

The stellar neutron capture cross sections of the stable $^{174}$Hf and the radioactive $^{182}$Hf have been measured for the first time. The resulting Maxwellian averaged cross sections at $kT =$ 30 keV are $\langle\sigma\rangle_{30} = 983 \pm 46$ mb for $^{174}$Hf and $\langle\sigma\rangle_{30} = 143 \pm 9$ mb for $^{182}$Hf. The experimental technique was cross-checked against the precise TOF values for $^{180}$Hf [14], which could be perfectly reproduced. Systematic uncertainties were carefully evaluated by repeated activations with systematically modified experimental conditions, i.e., by using different samples, proton beam currents, integrated neutron fluxes, and irradiation times.

Since no experimental data existed prior to this work, the present results were expected to represent an interesting test for theoretical predictions over a fairly long isotope chain. Though accurate cross sections were available for the isotopes between $^{176}$Hf and $^{180}$Hf, it turned out that even dedicated calculations with the Hauser-Feshbach statistical model were left with uncertainties of $\geqslant$30%.

The astrophysical consequences of the new cross section data apply mostly to the problem of the minimum in the $r$-process abundance distribution around $A = 180$, which suggests a smaller $r$ component of $^{182}$W than assumed before. If confirmed, this finding would strongly affect the chronometry of the early solar system in the sense that the time interval for formation of solid bodies would be significantly shorter than previously thought. To settle this important question, an accurate measurement of the stellar $(n, \gamma)$ cross sections of $^{182}$W and $^{184}$W is of highest priority.

## ACKNOWLEDGMENTS

We thank E. P. Knaetsch, D. Roller, and W. Seith for their help and support during the irradiations at the Van de Graaff accelerator. We are grateful to A. Mengoni, IAEA Vienna, T. Rauscher, University of Basel, T. Kawano, Los Alamos National Laboratory, A. Koning, NRG Petten , and M. Herman, NNDC Brookhaven, for providing their best predictions of

these cross sections for the presented comparison. This work was supported by the Swiss National Science Foundation Grant Nos. 2024-067428.01 and 2000-105328. R.G. and S.B. also acknowledge support by the Italian MIUR-FIRB Project "The astrophysical origin of the heavy elements beyond Fe."

[1] M. Busso, R. Gallino, and G. Wasserburg, Annu. Rev. Astron. Astrophys. **37**, 239 (1999).
[2] J. Audouze, W. Fowler, and D. Schramm, Nature (London) **238**, 8 (1972).
[3] M. Arnould, Astron. Astrophys. **22**, 311 (1973).
[4] H. Beer, F. Käppeler, K. Wisshak, and R. Ward, Astrophys. J. Suppl. **46**, 295 (1981).
[5] N. Klay, F. Käppeler, H. Beer, and G. Schatz, Phys. Rev. C **44**, 2839 (1991).
[6] K. Wisshak, F. Voss, C. Arlandini, F. Bečvář, O. Straniero, R. Gallino, M. Heil, F. Käppeler, M. Krtička, S. Masera *et al*., Phys. Rev. Lett. **87**, 251102 (2001).
[7] D. Belic, C. Arlandini, J. Besserer, J. de Boer, J. Carroll, J. Enders, T. Hartmann, F. Käppeler, H. Kaiser, U. Kneissl *et al*., Phys. Rev. C **65**, 35801 (2002).
[8] M. Rayet, M. Arnould, M. Hashimoto, N. Prantzos, and K. Nomoto, Astron. Astrophys. **298**, 517 (1995).
[9] T. Rauscher, A. Heger, R. Hoffman, and S. Woosley, Astrophys. J. **576**, 323 (2002).
[10] S. Woosley, D. Hartmann, R. Hoffman, and W. Haxton, Astrophys. J. **356**, 272 (1990).
[11] K. Takahashi and K. Yokoi, At. Data Nucl. Data Tables **36**, 375 (1987).
[12] H. Beer and R. Ward, Nature (London) **291**, 308 (1981).
[13] F. Käppeler, C. Arlandini, M. Heil, F. Voss, K. Wisshak, R. Reifarth, O. Straniero, R. Gallino, S. Masera, and C. Travaglio, Phys. Rev. C **69**, 055802 (2004).
[14] K. Wisshak, F. Voss, F. Käppeler, L. Kazakov, F. Bečvář, M. Krtička, R. Gallino, and M. Pignatari, Phys. Rev. C **73**, 045807 (2006).
[15] D. Lambert, Astron. Astrophys. Rev. **3**, 201 (1992).
[16] M. Arnould and S. Goriely, Phys. Rep. **384**, 1 (2003).
[17] C. Vockenhuber, F. Oberli, M. Bichler, I. Ahmad, G. Quitté, M. Meier, A. N. Halliday, D.-C. Lee, W. Kutschera, P. Steier *et al*., Phys. Rev. Lett. **93**, 0172501 (2004).
[18] C. Harper and S. Jacobsen, Geochim. Cosmochim. Acta **60**, 1131 (1996).
[19] D.-C. Lee and A. Halliday, Science **274**, 1876 (1996).
[20] Y.-Z. Qian, Prog. Part. Nucl. Phys. **50**, 153 (2003).
[21] B. S. Meyer and D. D. Clayton, Space Sci. Rev. **92**, 133 (2000).
[22] G. Wasserburg, M. Busso, R. Gallino, and K. Nollett, Nucl. Phys. **A777**, 5 (2006).
[23] K. Rosman and P. Taylor, Pure Appl. Chem. **70**, 217 (1998).
[24] P. J. Patchett, Geochim. Cosmochim. Acta **47**, 81 (1983).
[25] R. G. Helmer and C. W. Reich, Nucl. Phys. **A211**, 1 (1973).
[26] R. G. Helmer, R. C. Greenwood, and C. W. Reich, Nucl. Phys. **A168**, 449 (1971).
[27] L. Danielsson, Acta Chem. Scand. **19**, 1859 (1965).
[28] C. Vockenhuber, M. Bichler, W. Kutschera, A. Wallner, I. Dillmann, and F. Käppeler, Phys. Rev. C **74**, 057303 (2006).
[29] C. Vockenhuber, M. Bichler, W. Kutschera, A. Wallner, I. Dillmann, and F. Käppeler (to be published).
[30] W. Ratynski and F. Käppeler, Phys. Rev. C **37**, 595 (1988).
[31] S. Dababneh, N. Patronis, P. Assimakopoulos, J. Görres, M. Heil, F. F. Käppeler, D. Karamanis, S. O'Brien, and R. Reifarth, Nucl. Instrum. Methods A **517**, 230 (2004).
[32] H. Beer and F. Käppeler, Phys. Rev. C **21**, 534 (1980).
[33] A. Macchiacelli and E. Browne, Nucl. Data Sheets **69**, 903 (1993).
[34] R. Firestone, Nucl. Data Sheets **62**, 101 (1991).
[35] I. Ahmad, J. P. Greene, E. F. Moore, W. Kutschera, and C. Vockenhuber, Phys. Rev. C **70**, 047301 (2004).
[36] R. Firestone, Nucl. Data Sheets **65**, 589 (1992).
[37] Z. Chunmei, Nucl. Data Sheets **95**, 59 (2002).
[38] T. W. Burrows, Nucl. Data Sheets **68**, 635 (1993).
[39] H. Donghui, W. Pingsheng, C. Xilin, T. Weizhi, N. Bangfa, Z. Lanzhi, Z. Guiying, L. Cunxiong, and L. Likun, J. Radiol. Nucl. Chem. **265**, 499 (2005).
[40] J. Hubbell and S. Seltzer, Tables of X-Ray Mass Attenuation Coefficients and Mass Energy-Absorption Coefficients from 1 keV to 20 MeV for Elements $Z = 1$ to 92 and 48 Additional Substances of Dosimetric Interest (1996), http://physics.nist.gov/PhysRefData/XrayMassCoef/cover.html.
[41] CERN Tech. Rep., 2002 (unpublished), GEANT home page: http://wwwinfo.cern.ch/asd/geant4/geant4.html.
[42] Z. Bao, H. Beer, F. Käppeler, F. Voss, K. Wisshak, and T. Rauscher, At. Data Nucl. Data Tables **76**, 70 (2000).
[43] T. Rauscher and F.-K. Thielemann, At. Data Nucl. Data Tables **79**, 47 (2001).
[44] A. Koning (private communication).
[45] M. Herman (private communication).
[46] T. Rauscher and F.-K. Thielemann, At. Data Nucl. Data Tables **75**, 1 (2000).
[47] S. Goriely, in *Long Term Needs for Nuclear Data Development*, edited by M. Herman (International Atomic Energy Agency, Vienna, 2001), p. 83; Report INDC(NDS)-428 (unpublished).
[48] M. Herman, R. Capote-Noy, P. Obložinsky, A. Trkov, and V. Zerkin, J. Nucl. Sci. Technol. Suppl. **2**, 116 (2002).
[49] S. Goriely, Tech. Rep., 1998 (unpublished), http://www-astro.ulb.ac.be.
[50] C. Vockenhuber, M. Bichler, R. Golser, W. Kutschera, V. Liechtenstein, A. Priller, P. Steier, and S. Winkler, Nucl. Instrum. Methods B **223**, 823 (2004).
[51] K. Sonnabend, P. Mohr, K. Vogt, A. Zilges, A. Mengoni, T. Rauscher, H. Beer, F. Käppeler, and R. Gallino, Astrophys. J. **583**, 506 (2003).
[52] R. Schwengner, R. Beyer, F. Dönau, E. Grosse, A. Hartmann, A. Junghans, S. Mallion, G. Rusev, K. Schilling, and W. Schulze, Nucl. Instrum. Methods A **555**, 211 (2005).
[53] H. Utsunomiya, H. Akimune, S. Goko, M. Ohta, H. Ueda, T. Yamagata, K. Yamasaki, H. Ohgaki, H. Toyokawa, Y.-W. Lui *et al*., Phys. Rev. C **67**, 015807 (2003).
[54] S. Müller, M. Babilon, A. Zilges, M. Erhard, E. Grosse, A. Junghans, N. Nankov, A. Wagner, M. Heil, and F. Käppeler, Tech. Rep., GSI Darmstadt, 2004 (unpublished).
[55] K.-L. Kratz, J.-P. Bitouzet, F.-K. Thielemann, P. Möller, and B. Pfeiffer, Astrophys. J. **403**, 216 (1993).
[56] C. Freigburghaus, S. Rosswog, and F.-K. Thielemann, Astrophys. J. **525**, 121 (1999).
[57] I. Dillmann and R. Plag, Tech. Rep., Forschungszentrum Karlsruhe, 2005 (unpublished), http://nuclear-astrophysics.fzk.de/kadonis.

[58] R. Gallino, C. Arlandini, M. Busso, M. Lugaro, C. Travaglio, O. Straniero, A. Chieffi, and M. Limongi, Astrophys. J. **497**, 388 (1998).
[59] C. Arlandini, F. Käppeler, K. Wisshak, R. Gallino, M. Lugaro, M. Busso, and O. Straniero, Astrophys. J. **525**, 886 (1999).
[60] T. Kleine, C. Münker, K. Mezger, and H. Palme, Nature (London) **418**, 952 (2002).
[61] Q. Yin, S. Jacobsen, K. Yamashita, J. Blichert-Toft, P. Télouk, and F. Albarède, Nature (London) **418**, 949 (2002).
[62] R. Schoenberg, B. S. Kamber, K. D. Collerson, and O. Eugster, Geochim. Cosmochim. Acta **66**, 3151 (2002).
[63] G. Quitté, J. L. Birck, and A. N. Halliday, Geophys. Res. Abstr. **5**, 09643 (2003).
[64] A. N. Halliday, G. Quitté, and D.-C. Lee, Meteor. Planet. Sci. **38**, 5256 (2003).
[65] T. Kleine, K. Mezger, H. Palme, H. Scherer, and C. Münker, Geochim. Cosmochim. Acta **69**, 5805 (2005).
[66] G. Wasserburg, M. Busso, and R. Gallino, Astrophys. J. **466**, L109 (1996).